High-Resolution Laser-Induced Graphene. Flexible Electronics Beyond the Visible Limit

Article *in* ACS Applied Materials & Interfaces · February 2020

DOI: 10.1021/acsami.0c01377

7 authors, including:

Michael G Stanford
Rice University
41 PUBLICATIONS **433** CITATIONS
SEE PROFILE

Ilia N. Ivanov
Oak Ridge National Laboratory
246 PUBLICATIONS **5,078** CITATIONS
SEE PROFILE

James Tour
Rice University
852 PUBLICATIONS **69,714** CITATIONS
SEE PROFILE

ACS APPLIED MATERIALS & INTERFACES

Functional Nanostructured Materials (including low-D carbon)

High-Resolution Laser-Induced Graphene. Flexible Electronics Beyond the Visible Limit.

Michael G. Stanford, Cheng Zhang, Jason Davidson Fowlkes, Anna Hoffman, Ilia N. Ivanov, Philip D. Rack, and James M. Tour

ACS Appl. Mater. Interfaces, **Just Accepted Manuscript** • DOI: 10.1021/acsami.0c01377 • Publication Date (Web): 10 Feb 2020

is published by the American Chemical Society. 1155 Sixteenth Street N.W., Washington, DC 20036

High-Resolution Laser-Induced Graphene. Flexible Electronics Beyond the Visible Limit.

Michael G. Stanford,[1] Cheng Zhang,[2] Jason Davidson Fowlkes,[2,3] Anna Hoffman,[2] Ilia N. Ivanov,[3] Philip D. Rack,[2,3] James M. Tour[1,4,5,6*]*

[1]Department of Chemistry, Rice University, 6100 Main Street, Houston, Texas 77005, United States [2]Department of Materials Science and Engineering, University of Tennessee, Knoxville, TN 37996

[3]Center for Nanophase Materials Sciences, Oak Ridge National Laboratory, Oak Ridge, TN 37831

[4]Smalley-Curl Institute and the NanoCarbon Center, [5]Department of Materials Science and NanoEngineering, and [6]Department of Computer Science, Rice University, 6100 Main Street, Houston, Texas 77005, United States

Abstract Laser-induced graphene (LIG) is a multifunctional graphene foam that is commonly direct-written with an infrared laser into a carbon-based precursor material. Here, a visible 405 nm laser is used to directly convert polyimide into LIG. This enabled the formation of LIG with a spatial resolution of ~ 12 μm and a thickness of < 5 μm. The spatial resolution enabled by the relatively smaller focused spot size of the 405 nm laser represents a > 60% reduction in LIG feature sizes reported in prior publications. This process occurs *in situ* in an SEM chamber, thus allowing direct observation of LIG formation. The reduced size of the LIG features enables the direct-write formation of flexible electronics which are not visible to the unaided eye. A humidity sensor is demonstrated which could detect human breath with a response time of 250 ms. With the growing interest in LIG for flexible electronics and sensors, finer features can greatly expand its utility.

Keywords: Laser-induced graphene, high resolution, flexible sensor, visible laser

Introduction

Graphene, which is composed of 2-dimensional sp^2-hybridized carbon, has received much attention because of its exceptional physical, chemical, mechanical, and electrical properties.[1–5] Advances in graphene and graphene oxide synthesis techniques have enabled bulk synthesis[6–9] as well as the growth of large area graphene films.[10–12] Typically, chemical vapor deposition (CVD) methods are used to synthesize large area films of graphene and other 2D materials, which can subsequently be lithographically patterned to form electronic devices and sensors.[13]

Recently, lasers have been used to photothermally convert and pattern carbon precursors directly into graphene.[14–16] This material is called laser-induced graphene (LIG). LIG is composed of a percolating network of porous multi-layer graphene. LIG is distinct from simple laser carbonation of carbon precursors.[17] LIG can be formed by laser irradiating various carbon precursors including polyimide, polyethersulfone, wood, food, clothing, and paper,[18,19] to name a few. LIG is typically formed by an infrared laser scribing system (10.6 μm CO_2 laser) commonly found in machine shops. The IR laser couples to C-C bonds present in the carbon precursor and provides efficient photothermal heating. The rastering capabilities of these laser systems enables LIG to be readily patterned into desired geometries. This has enabled the direct-write formation and devices such as microsupercapacitors,[20–23] wearable sensors,[24,25] triboelectric nanogenerators,[26,27] gas sensors,[28] and battery cathodes.[29] Typically, LIG patterned with an IR laser system is limited to the spatial resolution of the focused IR laser, and due to the beam optics and diffraction limitations, a 10.6 μm CO_2 laser typically produces 60 – 100 μm linewidths. This prevents the formation of discrete LIG features that are invisible to the unaided eye. Due to the

smaller wavelengths, visible and ultraviolet (UV) lasers can be focused to much smaller spot sizes than IR lasers. Recent work has demonstrated that LIG can also be formed using an UV laser.[30] Additionally, visible 405 nm lasers have been demonstrated to form LIG from various carbon sources.[31,32] However, improved LIG resolution has yet to be demonstrated and the smallest LIG features formed directly from lasing are on the order of ~ 30-40 μm. [32,33]

In this work, LIG is formed by irradiating a polyimide (PI) substrate with a visible fiber-coupled 405 nm laser with a 1 e^{-2} radius of ~3 μm. The fiber-coupled 405 nm laser was mounted on an SEM chamber, which allowed *in situ* observation of the formation of LIG by secondary electron imaging. The LIG formation is localized to the top 5 μm of the substrate and a lateral resolution of ~12 μm is achieved. To the best of our knowledge, this represents > 60% reduction in previously published direct-write LIG feature size. With the rapidly growing interest in LIG patterns for flexible electronics and other applications,[15,16] finer feature sizes that are invisible to the eye could greatly expand the utility. The LIG exhibits a resistivity comparable to LIG formed by an IR-laser, the most common synthesis method. The high-resolution LIG is used to direct-write humidity sensors on a PI substrate, which has features invisible to the unaided eye. This represents an advancement in the application of LIG for discrete sensors or circuitry.

Results and Discussion

A fiber-coupled 405 nm visible laser was mounted in a high-angle port of a SEM chamber and focused on the stage to enable simultaneous laser exposure of PI and SEM imaging. *In situ* SEM videos for LIG formation can be found in the Supporting Information. Conveniently, PI strongly absorbs 405 nm photons (Figure S1), therefore making 405 nm lasers attractive for photothermally converting PI to LIG. Figure 1a shows a schematic of the experimental setup. The

laser system enables precise control of laser irradiance, pulse width, and frequency, and is discussed in more detail in previous publications[34,35] and the Methods section. In order to determine the critical fluence necessary for LIG formation with a 405 nm laser, a constant laser irradiance (834 kW cm^{-2}) was applied with varying laser pulse width. The relatively high laser irradiance is achieved with just a ~161 mW laser due to the small laser spot size (1 e^{-2} radius of ~3 μm). This low power laser is attractive for the ultimate commercialization of LIG. Figure 1b shows an optical image of PI exposed with varying pulse width. The heat affected zone (HAZ) of the laser scales with pulse width until saturation at pulse widths greater than ~1 ms, indicating saturation in photothermal heating. Figure 1c shows the Raman spectra for laser-irradiated spots as a function of pulse width. Below 100 μs pulse width, there is no obvious 2D Raman peak, thus indicating the photothermal heating was not sufficient to drive graphitization/LIG formation of the PI carbon source. Raman spectra for all pulse widths (2 μs – 100 ms) can be found in Figure S2. For pulse widths > 100 μs, the D, G, and 2D Raman peaks emerge, indicating the formation of LIG from the visible laser. The presence of a distinct 2D peak indicates that formation of graphitized carbon, and the single Lorentzian fit of the peak indicates the formation of graphene. The D-band and D + D' likely result from the bent graphene sheets in the LIG foam.[36] A threshold fluence (irradiance × pulse width) of 83.4 J cm^{-2} is required to form LIG from a single pulse laser exposure. The Raman background is reduced with increasing pulse width, which indicates that the LIG thickness is increasing and reducing the photoluminescent background from the PI substrate. For clarity, Figure 1d shows a rescaled Raman spectrum for LIG formed with a 1 ms pulse width. The influence of laser irradiance was also studied at a constant pulse width of 1 ms (Figure 1e). LIG is formed at irradiances > 186 kW cm^{-2}. Again, the decreasing Raman background suggests that the LIG thickness is increasing until it saturates above 480 kW cm^{-2}.

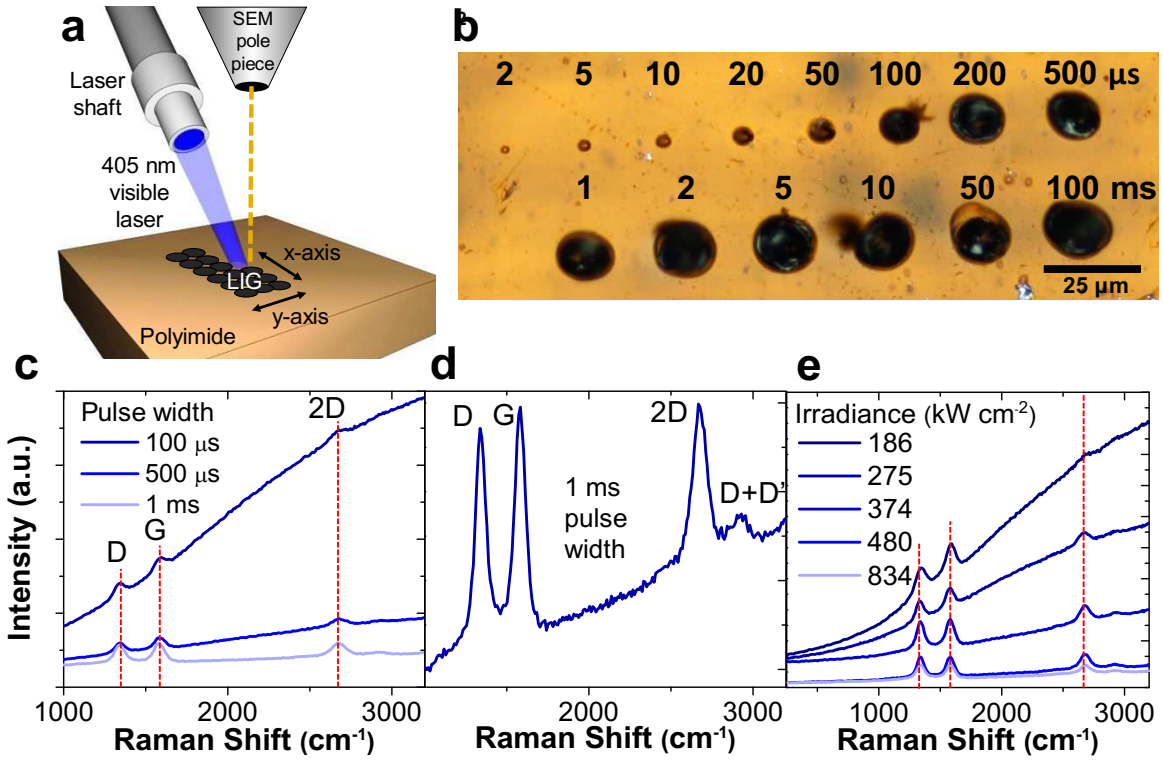

Figure 1. Laser condition studies. (a) Schematic of experimental setup that uses a 405 nm laser mounted on high-angle port of SEM. LIG is formed *in situ* in the SEM chamber. (b) Optical images of LIG formed from the 405 nm laser with pulse width varying from 2 µs to 100 ms. (c) Raman spectra of LIG formed at 834 kW cm^{-2} irradiance with pulse width greater than 100 µs. (d) Re-scaled Raman spectra of LIG formed with 1 ms pulse width. (e) Raman spectra of LIG formed at varying laser irradiance with a constant pulse width of 100 µs.

It is desirable to irradiate distinct patterns using a rastering technique in order to form functional devices from LIG. Typically, LIG is formed by an IR laser scribing system found in most machine shops. In these systems, a laser head with 2-dimensions of motion rasters as the laser is pulsed to generate a LIG pattern. For this work, the 405 nm pulsed laser position was fixed, and the SEM stage was moved to generate a raster pattern, and an approximate pixel overlap of

50% parallel and perpendicular to the major scanning direction was employed. The stage movement was synchronized with the laser pulses, such that the laser pulses after each stage movement. Figure 2a reports Raman spectra for LIG patterns made by the rastering technique with the 405 nm laser at varying laser irradiance with a constant 100 μs pulse width. Raster patterns irradiated with laser irradiance of > 480 kW cm^{-2} exhibited pronounced G, D, and 2D peaks, indicating the formation of LIG. The threshold for LIG formation for the raster patterns is 48 J cm^{-2}. This is lower than the threshold for a single laser pulse (83.4 J cm^{-2}) and indicates that overlap in the raster pattern reduces necessary fluence required for LIG formation. The effect of overlapping spots has been previously described in detail.[18] Figure 2b shows an SEM image of a LIG raster pattern generated with a laser pulse width of 100 μs and irradiance of 710 kW cm^{-2}. At lower laser irradiances, the LIG has a smoother morphology (Figure S3). With increasing laser irradiance (>480 kW cm^{-2}), LIG film roughness increases due to ablation at the center of the laser Gaussian peak. Figure 2c shows a high-resolution SEM image of the raster pattern, in which ablation of a smooth outer shell of residual PI can be seen where the peak of the laser Gaussian was irradiated. Inset arrows denote ablated regions. Supporting Information Figure S4 shows a high-resolution SEM suggesting that the LIG might be coated in a residual layer of PI, as made evident by the distinct surface texture. Overlay of a Raman map of the 2D/G ratio with the SEM image in Figure 2b, shows peaks in the 2D/G ratio that correspond to areas in which the outer PI shell was ablated away. Figures 2d-f report more 15 μm × 15 μm Raman maps of the 2D, G, and 2D/G ratio, respectively, for a LIG raster pattern generated with 710 kW cm^{-2} irradiance. Notably, the G peak is uniform, but the 2D peak is inhomogeneous and is the highest along the axis of the raster pattern where ablation of the surface PI layer occurs. This suggest that when lased with the 405 nm laser, LIG is formed in the near surface region, but may be encapsulated by a surface layer

of PI. This is further suggested by SEM images in Figure S5, in which charging patterns show that the LIG pattern is more conductive in regions where the top PI film was ablated.

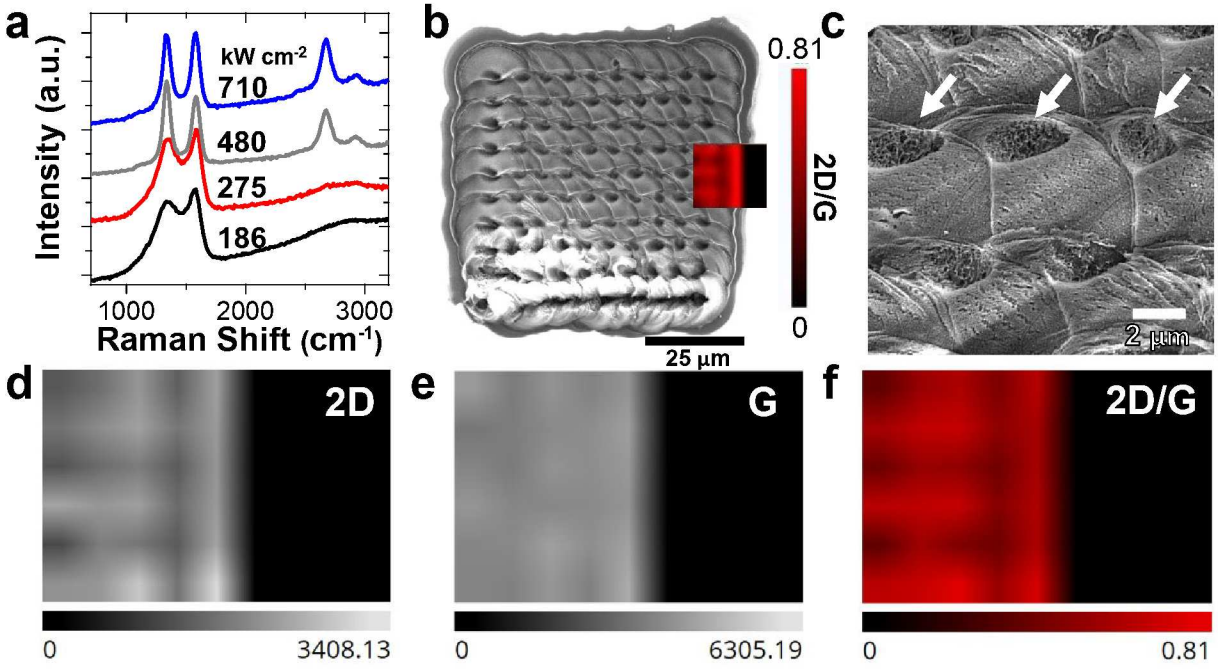

Figure 2. Raster patterns and Raman characterization. (a) Representative Raman spectra for LIG raster patterns of varying laser irradiance with 100 µs pulse width. (b) LIG raster pattern lased and 710 kW cm^{-2} irradiance with overlaid 2D/G Raman map. (c) High-resolution SEM image of LIG raster pattern showing (arrows) ablation of the PI shell at the peak of the laser Gaussian. Raman maps showing (d) 2D, (e) G, and (f) 2D/G peak intensity ratios. Maps are 15 µm × 15 µm in dimension. Variations in 2D/G ratio correspond with raster pattern pixels where ablation occurred.

Figures 3a-d show SEM images of lased PI patterns that were cross-sectioned with a focused Ga^+ ion beam. Raman spectra collected from the raster patterns are shown in Figures 3a,b and reveal signatures of amorphous carbon (Figure 2a), such as a broad D and G peak. Raman spectra of LIG patterns from Figure 3c,d exhibit a strong 2D peak indicative of LIG. Figure 3e is

a plot of the thickness of the HAZ as a function of laser irradiance. Notably, the minimum LIG thickness demonstrated was ~ 4.3 µm. LIG formed from IR laser sources is commonly ~25 – 50 µm in thickness. The visible 405 nm laser enables the more near-surface formation of LIG, which is comparable to LIG formed from a UV laser (~ 5 µm).[30] The near-surface conversion of carbon precursors to LIG is critical for the formation of discrete sensors and electronics without causing excessive damage to the substrate that compromises structural integrity.

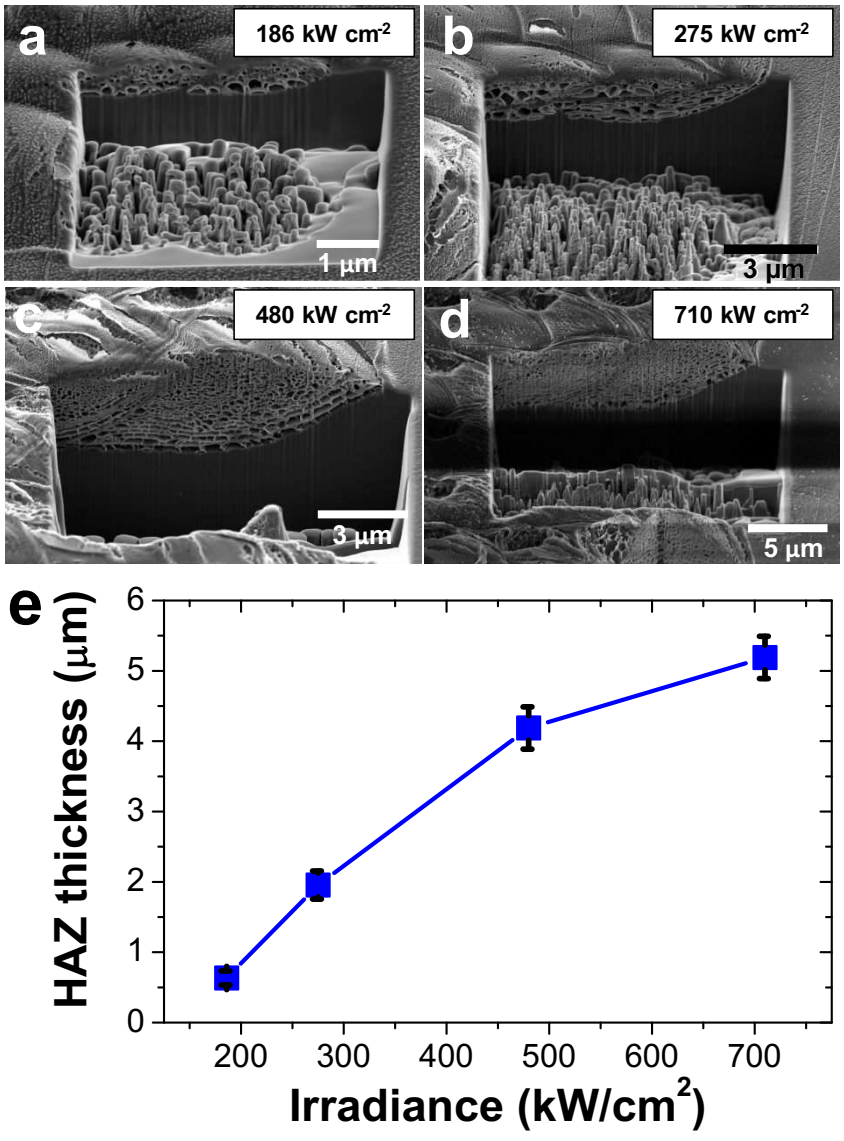

Figure 3. Thickness of LIG raster patterns. (a-d) Cross-sections of LIG raster patterns lased with varying laser irradiance with 50% pixel overlap. (e) Thickness of LIG raster patterns as a function of laser irradiance. Error bars denote standard deviation for the thickness measured at 5 points across the raster pattern.

The spatial resolution and electronic properties of LIG raster patterns formed from a visible laser were explored in Figure 4. Figure 4a shows optical images recorded for a LIG line pattern. Notably, the LIG pattern is invisible to the unaided eye (silver paste contacts are visible). The SEM image in Figure 4b shows that LIG lines with widths of ~13 μm and are formed using a 1-pixel-wide raster pattern. Additional lasing parameters can be found in the Methods section. The LIG resolution with the 405 nm laser represents a ~80 % improvement in LIG resolution reported to date. Figure 4c reports the width of LIG raster patterns that are 1 and 3 pixels wide as a function of laser irradiance, illustrating line width increases with irradiance. The sheet resistances of the LIG line patterns are reported in Figure 4d. The resistance decreases with increasing irradiance and saturates for irradiances beyond 480 kW cm^{-2}. This suggests that additional irradiance does little to improve the LIG quality. Sheet resistance as low as 108 Ω sq^{-1} is realized for LIG line patterns that are 3 pixels wide at an irradiance of 480 kW cm^{-2}. LIG sheet resistances have been reported as low as ~ 5 Ω/sq,[18] but the reduced thickness of the visible laser LIG is largely responsible for the higher sheet resistance value. The LIG resistivity here (108 Ω sq^{-1}) is comparable to typical LIG formed from an IR laser (60 – 100 Ω sq^{-1}).[14]

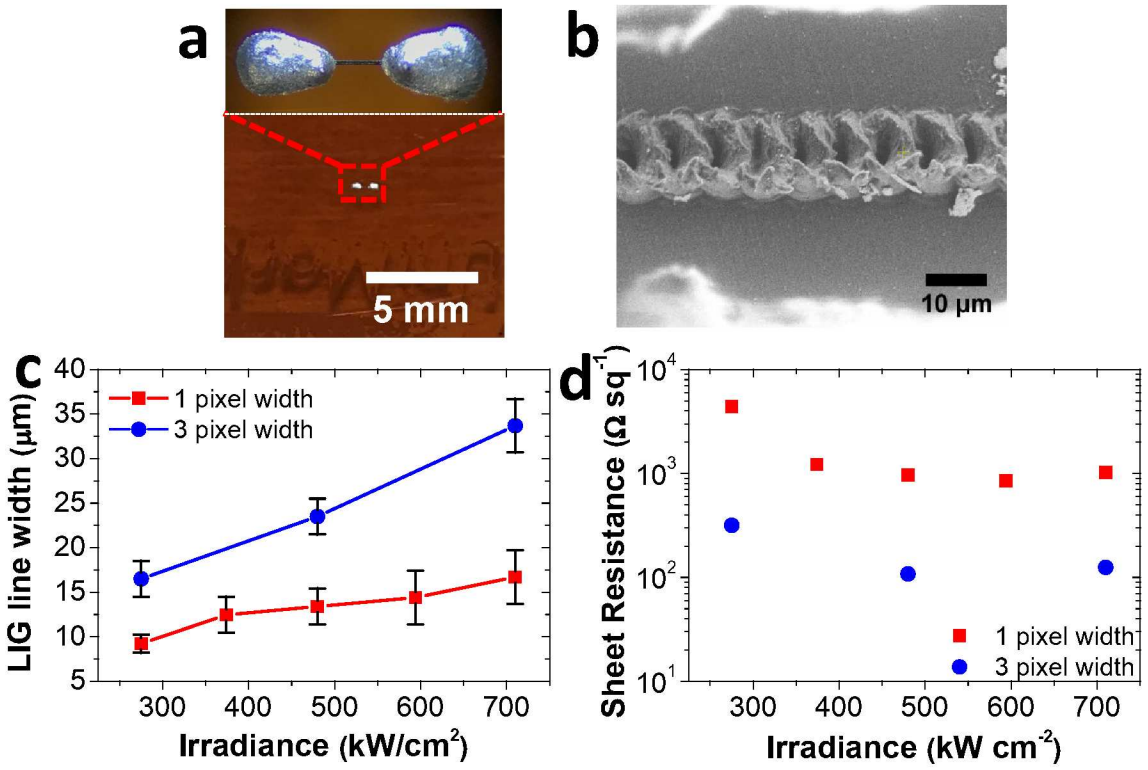

Figure 4. LIG line patterns and electrical characterization. (a) Optical images of LIG raster patterns generated with 1 pixel width. The image above is the expanded image in the red lower rectangle. (b) SEM image of LIG line pattern with 1 pixel width (~13 μm). (c) Width of LIG line patterns as a function of laser irradiance with 1 and 3 pixels raster width. Error bars represent standard deviation of LIG raster pattern width. (d) Sheet resistance of LIG line patterns.

To take advantage of the improved resolution, LIG line patterns were formed to generate a humidity sensor. Figure 5a shows the sensor schematic. LIG electrodes were patterned by rastering the 405 nm laser with an intentional micro-gap between the electrodes and a potential was applied across the electrodes. Previous work has shown that the adsorption of moisture in PI can significantly alter structural and electronic properties of the material.[37] In this device depicted in Figure 5a, the LIG electrodes are in close proximity (~7 μm), which allows precise monitoring of

the conductivity of the PI between the electrodes when exposed to moisture. Figure 5b shows an optical image of the micro-gap between the LIG electrodes which has a width of 7 μm, enabled by the improved LIG resolution with the 405 nm laser. Importantly, these sensors can be patterned in a high density on flexible substrates, such as PI (Figure 5c). The LIG patterns are invisible to the unaided eye and enable direct-write formation of discrete sensors and circuitry from graphene. When exposed to increased moisture content from human breath, the conductivity across the micro-gap increases due to adsorption of moisture on the PI film. Increased moisture adsorption results in a spike in the current between the electrodes under a constant bias (Figure 5d). A breath frequency of ~ 6 breaths/min was applied to allow the response and recovery of the sensor to be clearly observed. When exposed to human breath, the sensor has a response time of ~ 250 ms, where the response time is defined by the amount of time that it takes the sensor to reach > 90% of the peak current induced from exposure to moisture.

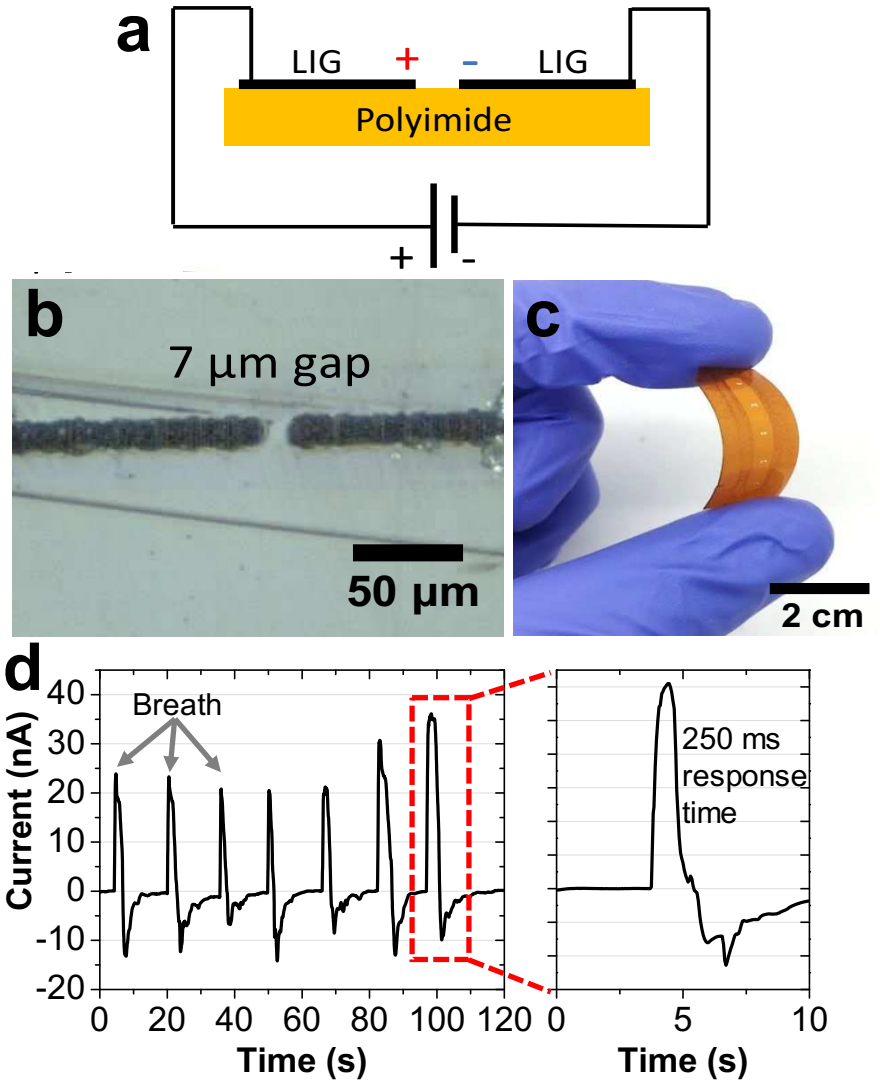

Figure 5. Non-visible humidity sensor formed from LIG. (a) Schematic of LIG humidity sensor with micro-gap channel. (b) Optical image of flexible humidity sensor on PI. (c) Optical image of micro-gap for LIG sensor. Visible particles on PI are silver epoxy contacts. (d) Response of LIG sensor to human breath. Response time of < 250 ms is exhibited.

Conclusions

In summary, a 405 nm laser with a 1 e^{-2} radius of ~ 3 µm was used to directly pattern PI into LIG. The small laser spot size enabled the formation of LIG line patterns with a width of ~12 µm, which

is a > 60% reduction in minimum LIG feature sizes reported formerly. The LIG exhibits sheets resistances (108 Ω sq^{-1}) comparable to LIG which is formed with the commonly used infrared laser. The small LIG feature sizes enabled the formation of flexible humidity sensors directly fabricated on PI, which were invisible to the unaided eye. The humidity sensors could sense human breath with a response time of 250 ms. The formation of LIG from smaller spot size visible lasers also enable lower power lasers (~161 mW) to be used which is attractive for ultimate commercialization of LIG. Reduced LIG feature sizes also expands the utility of LIG for flexible electronics and sensors.

Methods

Laser Delivery System:

The laser delivery system, developed by Waviks Inc., was mounted on a high-angle port of an SEM (FEI Nova Nanolab 600). The 405 nm laser diode is fed into the SEM chamber by a single-mode fiber. The laser was focused on the SEM substrate via miniature focusing lenses. Since the laser was mounted at a 52° angle relative to the substrate, the laser exhibits an elliptical shape. The 1 e^{-2} radius of the 405 nm laser is ~ 2.2 μm along the short axis and ~ 2.8 μm along the long axis. Therefore, the smallest diameter LIG spots formed with this laser system should be on the order of ~6 μm at optimal focus. Peak optical power output for the 405 nm laser diode is 161 mW, which corresponds to an average irradiance of 834 kW cm^{-2}. A detailed description of the laser delivery system can be found elsewhere,[34] and a photograph can be found in **Figure S6**. In this work, the pulse width was tuned from 2 μs – 100 ms using a laser pulse generator. The 405 nm laser was used to lase commercial PI (McMaster-Carr) in order to form LIG.

Instruments:

LIG patterns were characterized by Raman spectroscopy on a Renishaw InVia Raman microscope. SEM images were collected of LIG patterns on a FEI Nova Nanolab 600 and FEI Helios SEM. UV-vis spectra were performed on a Shimadzu UV-3600 Plus. Electrical characterization of LIG was performed in a Desert Cryogenics model CPX-VF vacuum probe station. Electrical measurements were conducted with an Agilent Semiconductor Parameter Analyzer model B1500A

Supporting information

Video of *in situ* LIG formation. Optical absorbance and transmittance of polyimide. Raman spectra for LIG generated with various laser conditions. SEM images of Raman spectra of LIG raster patterns. Photographs of experimental setup.

AUTHOR INFORMATION

Corresponding authors

*E-mail: Philip D. Rack – prack@utk.edu, James M. Tour – tour@rice.edu

ORCID

Michael G. Stanford - 0000-0001-9663-1138

Cheng Zhang - 0000-0001-6531-4703

Anna N. Hoffman - 0000-0003-2899-0889

Ilia N. Ivanov - 0000-0002-6726-2502

Philip D. Rack - 0000-0002-9964-3254

Jason D. Fowlkes - 0000-0002-6295-5115

James M. Tour - 0000-0002-8479-9328

Acknowledgements

C.Z., A.H., and P.D.R. acknowledge support from the U.S. Department of Energy (DOE) under Grant No. DE-SC0002136. The authors acknowledge that the graphene synthesis and some of the Raman measurements were performed in the Nanofabrication Research Laboratory at the Center for Nanophase Materials Sciences, which is a DOE Office of Science User Facility and provides support for J.D.F, I.N.I and P.D.R. M.G.S. and J.M.T. acknowledge the Air Force Office of Scientific Research (FA9550-19-1-0296) for providing funding. The use of the LIG sensor to detect humidity from human breath in this work did not meet the definition of human subject research at Rice University, therefore no IRB protocol approval was needed.

Competing Interests

Rice University owns intellectual property on LIG. Some of that property has been licensed to a company in which J.M.T. is a stockholder, though not an officer or director. Conflicts of interest are managed through regular disclosures to the Rice University Office of Sponsored Programs and Research Compliance.

References

(1) Neto, A. H. C.; Guinea, F.; Peres, N. M. R.; Novoselov, K. S.; Geim, A. K. The Electronic Properties of Graphene. *Rev. Mod. Phys.* **2009**, *81*, 109.

(2) Zhu, Y.; Murali, S.; Cai, W.; Li, X.; Suk, J. W.; Potts, J. R.; Ruoff, R. S. Graphene and Graphene Oxide: Synthesis, Properties, and Applications. *Adv. Mater.* **2010**, *22*, 3906–3924.

(3) Falkovsky, L. A. Optical Properties of Graphene. In *Journal of Physics: Conference Series*; IOP Publishing, 2008; Vol. 129, p. 12004.

(4) Pop, E.; Varshney, V.; Roy, A. K. Thermal Properties of Graphene: Fundamentals and Applications. *MRS Bull.* **2012**, *37*, 1273–1281.

(5) Frank, I. W.; Tanenbaum, D. M.; van der Zande, A. M.; McEuen, P. L. Mechanical Properties of Suspended Graphene Sheets. *J. Vac. Sci. Technol. B Microelectron. Nanom. Struct. Process. Meas. Phenom.* **2007**, *25*, 2558–2561.

(6) Choucair, M.; Thordarson, P.; Stride, J. A. Gram-Scale Production of Graphene Based on Solvothermal Synthesis and Sonication. *Nat. Nanotechnol.* **2009**, *4*, 30.

(7) Luong, D. X.; Bets, K. V.; Algozeeb, W. A.; Stanford, M. G.; Kittrell, C.; Chen, W.; Salvatierra, R. V.; Ren, M.; McHugh, E. A.; Advincula, P. A.; Wang, Z.; Bhatt, M.; Guo, H.; Mancevski, V.; Shahsavari, R.; Yakobson, B.; Tour, J. M. Gram-Scale Bottom-up Flash Graphene Synthesis. *Nature* **2020**, *577*, 647-651.

(8) Marcano, D. C.; Kosynkin, D. V; Berlin, J. M.; Sinitskii, A.; Sun, Z.; Slesarev, A.; Alemany, L. B.; Lu, W.; Tour, J. M. Improved Synthesis of Graphene Oxide. *ACS Nano* **2010**, *4*, 4806–4814.

(9) Tour, J. M. Layered Materials: Scaling up Exfoliation. *Nat. Mater.* **2014**, *13*, 545.

(10) Li, X.; Cai, W.; An, J.; Kim, S.; Nah, J.; Yang, D.; Piner, R.; Velamakanni, A.; Jung, I.; Tutuc, E. Large-Area Synthesis of High-Quality and Uniform Graphene Films on Copper Foils. *Science.* **2009**, *324*, 1312–1314.

(11) Li, X.; Zhu, Y.; Cai, W.; Borysiak, M.; Han, B.; Chen, D.; Piner, R. D.; Colombo, L.; Ruoff, R. S. Transfer of Large-Area Graphene Films for High-Performance Transparent Conductive Electrodes. *Nano Lett.* **2009**, *9*, 4359–4363.

(12) Vlassiouk, I. V; Stehle, Y.; Pudasaini, P. R.; Unocic, R. R.; Rack, P. D.; Baddorf, A. P.; Ivanov, I. N.; Lavrik, N. V; List, F.; Gupta, N. Evolutionary Selection Growth of Two-

Dimensional Materials on Polycrystalline Substrates. *Nat. Mater.* **2018**, *17*, 318.

(13) Stanford, M. G.; Rack, P. D.; Jariwala, D. Emerging Nanofabrication and Quantum Confinement Techniques for 2D Materials beyond Graphene. *npj 2D Mater. Appl.* **2018**, *2*, 20.

(14) Lin, J.; Peng, Z.; Liu, Y.; Ruiz-Zepeda, F.; Ye, R.; Samuel, E. L. G.; Yacaman, M. J.; Yakobson, B. I.; Tour, J. M. Laser-Induced Porous Graphene Films from Commercial Polymers. *Nat. Commun.* **2014**, *5*, 5714.

(15) Ye, R.; James, D. K.; Tour, J. M. Laser-Induced Graphene: From Discovery to Translation. *Adv Mater* **2018**, *31*, 1803621.

(16) Ye, R.; James, D. K.; Tour, J. M. Laser-Induced Graphene. *Acc. Chem. Res.* **2018**, *51*, 1609–1620.

(17) In, J. Bin; Hsia, B.; Yoo, J. H.; Hyun, S.; Carraro, C.; Maboudian, R.; Grigoropoulos, C. P. Facile Fabrication of Flexible All Solid-State Micro-Supercapacitor by Direct Laser Writing of Porous Carbon in Polyimide. *Carbon* **2015**, *83*, 144–151.

(18) Chyan, Y.; Ye, R.; Li, Y.; Singh, S. P.; Arnusch, C. J.; Tour, J. M. Laser-Induced Graphene by Multiple Lasing: Toward Electronics on Cloth, Paper, and Food. *ACS Nano* **2018**, *12*, 2176–2183.

(19) Ye, R.; Chyan, Y.; Zhang, J.; Li, Y.; Han, X.; Kittrell, C.; Tour, J. M. Laser-Induced Graphene Formation on Wood. *Adv. Mater.* **2017**, *29*, 1702211.

(20) Lamberti, A.; Clerici, F.; Fontana, M.; Scaltrito, L. A Highly Stretchable Supercapacitor Using Laser-Induced Graphene Electrodes onto Elastomeric Substrate. *Adv. Energy Mater.* **2016**, *6*, 1600050.

(21) Li, L.; Zhang, J.; Peng, Z.; Li, Y.; Gao, C.; Ji, Y.; Ye, R.; Kim, N. D.; Zhong, Q.; Yang, Y.

High-Performance Pseudocapacitive Microsupercapacitors from Laser-Induced Graphene. *Adv. Mater.* **2016**, *28*, 838–845.

(22) Peng, Z.; Ye, R.; Mann, J. A.; Zakhidov, D.; Li, Y.; Smalley, P. R.; Lin, J.; Tour, J. M. Flexible Boron-Doped Laser-Induced Graphene Microsupercapacitors. *ACS Nano* **2015**, *9*, 5868–5875.

(23) Peng, Z.; Lin, J.; Ye, R.; Samuel, E. L. G.; Tour, J. M. Flexible and Stackable Laser-Induced Graphene Supercapacitors. *ACS Appl. Mater. Interfaces* **2015**, *7*, 3414–3419.

(24) Sun, B.; McCay, R. N.; Goswami, S.; Xu, Y.; Zhang, C.; Ling, Y.; Lin, J.; Yan, Z. Gas-Permeable, Multifunctional On-Skin Electronics Based on Laser-Induced Porous Graphene and Sugar-Templated Elastomer Sponges. *Adv. Mater.* **2018**, *30*, 1804327.

(25) Tao, L.-Q.; Tian, H.; Liu, Y.; Ju, Z.-Y.; Pang, Y.; Chen, Y.-Q.; Wang, D.-Y.; Tian, X.-G.; Yan, J.-C.; Deng, N.-Q.; Yang, Y.; Ren, T.-L. An Intelligent Artificial Throat with Sound-Sensing Ability Based on Laser Induced Graphene. *Nat. Commun.* **2017**, *8*, 14579.

(26) Stanford, M. G.; Li, J. T.; Chyan, Y.; Wang, Z.; Wang, W.; Tour, J. M. Laser-Induced Graphene Triboelectric Nanogenerators. *ACS Nano* **2019**, *13*, 7166–7174.

(27) Luo, J.; Fan, F. R.; Jiang, T.; Wang, Z.; Tang, W.; Zhang, C.; Liu, M.; Cao, G.; Wang, Z. L. Integration of Micro-Supercapacitors with Triboelectric Nanogenerators for a Flexible Self-Charging Power Unit. *Nano Res.* **2015**, *8*, 3934–3943.

(28) Stanford, M. G.; Yang, K.; Chyan, Y.; Kittrell, C.; Tour, J. M. Laser-Induced Graphene for Flexible and Embeddable Gas Sensors. *ACS Nano* **2019**, *13*, 3474–3482.

(29) Ren, M.; Zhang, J.; Tour, J. M. Laser-Induced Graphene Hybrid Catalysts for Rechargeable Zn-Air Batteries. *ACS Appl. Energy Mater.* **2019**, *2*, 1460–1468.

(30) Carvalho, A. F.; Fernandes, A. J. S.; Leitão, C.; Deuermeier, J.; Marques, A. C.; Martins,

R.; Fortunato, E.; Costa, F. M. Laser-Induced Graphene Strain Sensors Produced by Ultraviolet Irradiation of Polyimide. *Adv. Funct. Mater.* **2018**, *28*, 1805271.

(31) Zhang, Z.; Song, M.; Hao, J.; Wu, K.; Li, C.; Hu, C. Visible Light Laser-Induced Graphene from Phenolic Resin: A New Approach for Directly Writing Graphene-Based Electrochemical Devices on Various Substrates. *Carbon* **2018**, *127*, 287–296.

(32) Romero, F.; Salinas-Castillo, A.; Rivadeneyra, A.; Albrecht, A.; Godoy, A.; Morales, D.; Rodriguez, N. In-Depth Study of Laser Diode Ablation of Kapton Polyimide for Flexible Conductive Substrates. *Nanomaterials* **2018**, *8*, 517.

(33) Bobinger, M. R.; Romero, F. J.; Salinas-Castillo, A.; Becherer, M.; Lugli, P.; Morales, D. P.; Rodríguez, N.; Rivadeneyra, A. Flexible and Robust Laser-Induced Graphene Heaters Photothermally Scribed on Bare Polyimide Substrates. *Carbon* **2019**, *144*, 116–126.

(34) Wu, Y.; Liu, C.; Moore, T. M.; Magel, G. A.; Garfinkel, D. A.; Camden, J. P.; Stanford, M. G.; Duscher, G.; Rack, P. D. Exploring Photothermal Pathways *via in Situ* Laser Heating in the Transmission Electron Microscope: Recrystallization, Grain Growth, Phase Separation, and Dewetting in Ag 0.5 Ni 0.5 Thin Films. *Microsc. Microanal.* **2018**, *24*, 647–656.

(35) Stanford, M. G.; Mahady, K.; Lewis, B. B.; Fowlkes, J. D.; Tan, S.; Livengood, R.; Magel, G. A.; Moore, T. M.; Rack, P. D. Laser-Assisted Focused He + Ion Beam Induced Etching with and without XeF_2 Gas Assist. *ACS Appl. Mater. Interfaces* **2016**, *8*, 29155–29162.

(36) Dimiev, A. M.; Ceriotti, G.; Behabtu, N.; Zakhidov, D.; Pasquali, M.; Saito, R.; Tour, J. M. Direct Real-Time Monitoring of Stage Transitions in Graphite Intercalation Compounds. *ACS Nano* **2013**, *7*, 2773–2780.

(37) Buchhold, R.; Nakladal, A.; Gerlach, G.; Sahre, K.; Müller, M.; Eichhorn, K. J.; Herold, M.; Gauglitz, G. A Study on the Microphysical Mechanisms of Adsorption in Polyimide

Layers for Microelectronic Applications. *J. Electrochem. Soc.* **1998**, *145*, 4012–4018.

Table of Contents Graphic